Journal of The Electrochemical Society, **157** (6) H598-H602 (2010)
0013-4651/2010/157(6)/H598/5/$28.00 © The Electrochemical Society

Phase and Optical Characterizations of Annealed SnO Thin Films and Their p-Type TFT Application

Ling Yan Liang, Zhi Min Liu, Hong Tao Cao,[z] Zheng Yu, Yuan Yuan Shi, Ai Hua Chen, Hai Zhong Zhang, Yan Qun Fang, and Xi Lian Sun

Division of Functional Materials and Nano Devices, Ningbo Institute of Material Technology and Engineering, Chinese Academy of Sciences, Ningbo 315201, People's Republic of China

Amorphous SnO thin films were prepared on quartz and 190 nm SiO_2/Si(001) substrates by electron beam evaporation. X-ray diffraction results reveal that amorphous SnO transforms into polycrystalline α-SnO (tetragonal litharge structure) after rapid thermal annealing in Ar ambient at 350–400°C and starts decomposing into *o*-SnO_2 (orthorhombic structure) with the expulsion of Sn atoms at 450–500°C. The optical properties were characterized via spectroscopic ellipsometry. The polycrystalline SnO thin films have a higher refractive index n and a narrower bandgap E_g than the amorphous ones, which is due to the polarizability enhancement in the crystallization process. Moreover, the relationship between n and E_g of the amorphous and polycrystalline SnO thin films can be explained by the "Moss rule" law, and a decreasing trend in n was verified with the transformation from SnO to SnO_2. Bottom-gate-type thin film transistors (TFTs) employing polycrystalline SnO channels on the SiO_2/Si(001) substrates exhibit p-type field-effect transistor characteristics. The optimum field-effect mobilities μ_{sat} and μ_{lin} are 0.46 and 0.87 $cm^2\ V^{-1}\ s^{-1}$, respectively, which are the same order of magnitude as those reported for epitaxial SnO TFTs.
 [DOI: 10.1149/1.3385390]

Manuscript submitted December 3, 2009; revised manuscript received March 8, 2010. Published April 19, 2010.

Over decades, tin monoxide (SnO) has been studied as the anode material,[1] coating substance,[2] gas sensitive material,[3] catalyst,[4] and precursor for the production of tin oxide (SnO_2).[5,6] Recently, SnO has attracted attention simply because of an advantage of high hole mobility in the application of p-type oxide devices.[7] It has been proposed that the valence band maxima (VBM) of SnO are mainly contributed by Sn 5s orbitals.[8-10] Isotropic extended s orbitals constitute largely overlapped wave functions of the cations, which form effective carrier conduction paths; thus, SnO exhibits a fairly high hole mobility compared with other p-type conductive oxides,[7] such as NiO,[11] ZnO,[12] and SnO_2,[13,14] of which the VBM are mainly made of rather localized O 2p orbitals.[10,15-17] Moreover, the p-type conductivity of SnO was suggested to originate from the tin vacancy,[10,18] and it can be improved via proper doping.[19] Those properties make SnO a promising candidate to be a p-type oxide semiconductor utilized for applications in areas such as photovoltaics, electronics, displays, sensors, and information storage. The successful fabrication of p-channel thin film transistors (TFTs) based on SnO films has been reported,[7,20] and the maximum field-effect mobility ($1.3\ cm^2\ V^{-1}\ s^{-1}$) is 1 order of magnitude larger than those reported for a p-type Cu_2O TFT and a NiO TFT.[21,22]

SnO thin films have been fabricated by oxidating metal Sn,[23,24] directly evaporating a SnO raw material,[7] and decomposing a SnO_2 source material.[6,18] In those processes, impurity phases such as Sn and SnO_2 are hardly avoidable, which puts a burden on "pure" SnO film fabrication. SnO is metastable because of the following reasons. SnO decomposes at suitable temperatures even in the absence of oxygen following the disproportionation reaction[25-27]

$$2SnO \rightarrow SnO_2 + Sn \qquad [1]$$

However, SnO oxidizes in an oxygen-contained atmosphere by an internal displacement of oxygen (disproportionation reaction), followed by an incorporation of external oxygen.[5,6,27] Generally, the phase transformation from SnO to SnO_2 is dependent on many factors such as the film preparation method and conditions, the post-thermal treatment method, atmosphere, duration, and temperature. Among them, the temperature effect on the phase transformation is intensively investigated,[5,26,27] whereas the effects of other factors are seldom studied and need to be further investigated. A case in point is that the phase transformations of SnO are mainly studied by conventional annealing but are scarcely investigated by rapid thermal annealing (RTA), which is a convenient and economic post-treatment method for device fabrication.

An accurate determination of the optical parameters, such as the refraction index n as well as the optical bandgap E_g, is an essential prerequisite for optoelectronic applications. However, the previous studies mainly focused on the variations of n and E_g with respect to the phase transformation from SnO to SnO_2.[24,28,29] Both the increasing and decreasing trends of n with the reduction of SnO fraction were reported,[24,28] which is quite controversial and needs to be clarified. Additionally, the differences between the reported values of E_g are particularly noticeable (2.5–3.4 eV),[6,30] and the large data scattering was supposed to result from the variation of the composition or impurity phases involved.[30] However, no unambiguous evidence has been given for those assertions. Therefore, further studies on the optical constant dispersion of SnO thin films are needed.

In this work, amorphous SnO thin films were grown by electron-beam evaporation at room temperature (RT), and their phase structural evolution after RTA treatment in Ar at different temperatures was investigated. Then, the relationship between the optical properties and the phase characteristics of the obtained films were analyzed. Finally, TFTs using the obtained films were fabricated as channels and their electrical properties were presented.

Experimental

Film preparation and characterization.— Before being loaded into an electron-beam evaporation ultrahigh vacuum (UHV) system, single-side-polished quartz wafers and Si substrates (with SiO_2 layers of 190 nm) were ultrasonically cleaned in sequence with acetone, ethanol, and deionized water and were eventually dried in N_2 gas flow. After evacuating to 5.0×10^{-6} Pa, SnO thin films were evaporated from a high purity SnO_2 source with a substrate temperature at RT (the films were labeled with F-deposited). A detailed description of the experimental procedure and the chemical composition analysis of the F-deposited film were reported elsewhere.[31] The [Sn]/[O] ratio was 49.5/50.5, which is close to the ideal stoichiometric ratio of SnO.

Subsequently, RTA was carried out at 300–500°C with intervals of 50°C for 10 min in Ar ambient (the films were labeled as RTA-300 to RTA-500, correspondingly). Vacuum annealing (VA) was also performed on the as-deposited film at 600°C for 30 min in a chamber with base pressure of about 2.0×10^{-4} Pa (the film was labeled as VA-600). As single-phase polycrystalline SnO thin films ([Sn]/[O] = 49.7/50.3) could be obtained by the VA treatment,[31] the

[z] E-mail: h_cao@nimte.ac.cn

film VA-600 of good crystallinity is used in this work as a reference to evaluate and compare the phase composition and optical properties of the RTA-treated films.

The crystal structures of the films were examined by X-ray diffraction (XRD) in the symmetric-reflection-coupled θ-2θ arrangement. XRD patterns were recorded on a Bruker D8 Advance X-ray diffractometer using Cu Kα radiation (λ_0 = 1.5418 Å). The thicknesses and the optical properties were analyzed via a variable angle spectroscopic ellipsometer (SE, J.A. Woollam Co., Inc.). The ellipsometric angle ψ and phase difference Δ were recorded in the wavelength range of 300–1700 nm at incidence angles of 55, 65, and 75°. The refraction index n and extinction coefficient k were obtained by fitting the spectroscopic spectra of ψ and Δ as a function of the incident wavelength λ. A simple optical model consisting of a quartz substrate, a bottom bulk SnO_x layer, and a surface roughness layer composed of 50% SnO_x and 50% void was used in the simultaneous fitting of the measured parameters. To simplify the fitting process, the spectra were divided into two regions. The Cauchy dispersion relation and the empirical Urbach relation were used to generate the SnO_x optical constants in λ = 500–1700 nm.[32,33] The global fit for the refractive index n, extinction coefficient k, and thickness over a wide range of possible values was performed to prevent the mean squared error from falling into a local minimum. The thicknesses of the surface roughness layer and the SnO_x film, hence obtained, were used to generate the optical constants in λ = 300–500 nm by a point-by-point fit. The light cannot penetrate into the substrate due to the strong absorption above the absorption edge (~500 nm for SnO thin films), and thus little influence come from the substrate, in which case, the point-by-point fitting results can be used.[32,34]

TFT fabrication and characterization.— Bottom-gate-type TFTs were fabricated using 100 nm thick as-deposited and RTA-treated films as channels, heavily doped p-type silicon as substrate and gate electrode, and thermally oxidized 190 nm thick SiO_2 layer as gate dielectric (the gate capacitance per unit area C_0 = 17 nF/cm^2). Ni/Au (30/50 nm) contact pads were evaporated on the top of the SnO_x films through a shadow mask at RT in the electron-beam evaporation UHV system. The length (L) and width (W) of the channels were 150 and 7500 μm, respectively.

The electrical properties of the channels were studied by the Hall effect measurement system (ACCENT, HL5500). Output and transfer characteristics of the TFTs were measured using a semiconductor parameter analyzer (Keithley 4200) at RT in the dark. Saturation mobility (μ_{sat}), linear mobility (μ_{lin}), and subthreshold voltage swing (S) were estimated using the following relations: $\mu_{sat} = 2LI_{DS}/WC_0(V_G - V_{th})^2$, $\mu_{lin} = (dI_{DS}/dV_G)(L/WC_0V_{DS})$, and $S = dV_G/d(\log I_{DS})$, where I_{DS}, V_G, V_{DS}, and V_{th} are the drain–source current, the gate bias, the drain bias, and the threshold voltage, respectively. The V_{th} were estimated from the $(-I_{DS})^{1/2}$ vs V_G plots.

Results and Discussion

Phase transformations.— XRD analysis was performed to study the crystal structures of the obtained films on quartz, as displayed in Fig. 1. For the films F-deposited and RTA-300, no extra peaks are found except the strong background, indicating the amorphous nature of the films. For films RTA-350, RTA-400, and VA-600, all the diffraction peaks can be indexed to α-SnO phase (α-PbO structure, P4/nmm, JCPDS card no. 06-0395); nevertheless, a slight shift to higher diffraction angles is observed compared with the standard powder values, revealing the presence of residual stress in the SnO grains. Table I presents a summary of the measured spacings (d_m) for the three samples and their deviation from the literature reported values (d_I). With increasing annealing temperature, the deviations of the d_m from the d_I for α-SnO reflections get smaller, implying the relaxed strain and the improved crystal quality of SnO grains.

The XRD patterns show the coexistence of α-SnO, orthorhombic SnO_2 (o-SnO_2, JCPDS card no. 29-1484), and Sn (JCPDS card no. 19-1365) in the film RTA-450 and the disappearance of the α-SnO phase in the film RTA-500, which suggests that the disproportionation Reaction 1 takes place during RTA treatment in Ar at 450°C and finishes at 500°C. Notice that metastable o-SnO_2 rather than stable γ-SnO_2 (tetragonal rutile structure, $P4_2/mnm$, JCPDS card no. 41-1445) appears, while the γ-SnO_2 phase is generally observed during conventional annealing treatment.[5,6,25-27] The above results support the assertion quite well that o-SnO_2 formation is favored in the annealing of disordered (amorphous or nanoparticle) tin oxide under oxygen-deficient conditions.[35-37] Additionally, intermediate products (Sn_2O_3 or Sn_3O_4) after the RTA are not detected, which is also quite different from the results using conventional annealing method.[5,6,25-27]

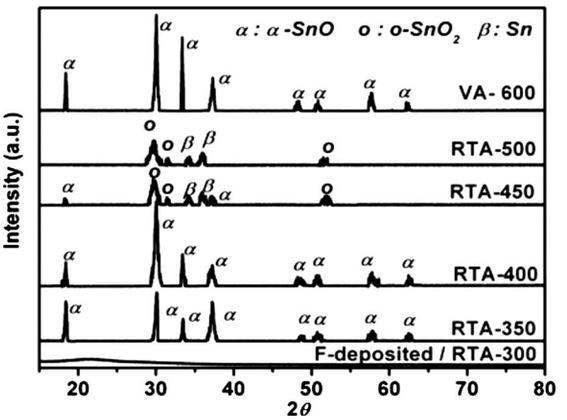

Figure 1. XRD patterns of the obtained SnO_x films. The background has been subtracted for clarity.

Optical properties.— The refractive index n for the obtained films as a function of incident wavelengths is presented in Fig. 2. The values of n of polycrystalline SnO (2.40–3.09) are much larger than those of amorphous SnO (2.23–2.93) in λ = 400–1700 nm. Generally, the refractive index of a thin film increases with increasing density or/and increasing local polarizability.[38] However, according to the SE fitting results, the surface roughness of the polycrystalline SnO films (15–25 nm) are larger than those of the amorphous ones (<5 nm), implying the smaller density of the polycrystalline films;[38,39] meanwhile, outdiffusion of oxygen in the annealing process (in accordance with the [Sn]/[O] ratio result presented in the experimental section) would increase the porosity of the oxide films, also resulting in a decrease in the polycrystalline film density.[40] Thus, the density can be excluded from the possible factors that affect the refractive index in the present case.

The relationship between the microscopic polarizability $p(r)$ and the macroscopic refractive index n is known as the Lorenz–Lorentz equation[41]

$$p(r) = \frac{3}{4\pi N}\left(1 - \frac{3}{n^2 + 2}\right) \qquad [2]$$

where N is the number density of molecules, and a higher value of n corresponds to a larger $p(r)$. From the discussions mentioned above, the large n of polycrystalline SnO could be due to the polarizability enhancement in the crystallization process. Shportko et al. also observed the similar phenomena in the phase-change crystalline materials.[42] They attributed the polarizability enhancement to the resonance bonding effect in the crystalline phase. In contrast to the pair bond formed by the nearest neighbors, resonant bonding requires the second and higher neighbors to be aligned, which is impossible in the amorphous phase. It has been reported that the resonance bonding also leads to the large $\varepsilon_\infty(\varepsilon_\infty = n^2)$ observed in many crystalline IV-VI compounds such as PbS and SnTe.[43] SnO, as one of the IV-VI compounds, could have similar property. Furthermore,

Table I. Comparison of measured (d_m) and literature reported (d_I) spacings determined from the XRD peak positions of the reflections for films RTA-350, RTA-400, and VA-600.

	RTA-350		RTA-400		VA-600	
Reflection	d_m (Å)	$(d_I - d_m)/d_I$ (%)	d_m (Å)	$(d_I - d_m)/d_I$ (%)	d_m (Å)	$(d_I - d_m)/d_I$ (%)
001	4.85	0.7	4.814	0.7	4.85	0.6
101	2.989	0.6	2.975	0.5	2.989	0.4
110	2.688	0.4	2.679	0.3	2.688	0.2
002	2.418	0.2	2.413	0.2	2.418	0.4
200	1.888	0.7	1.888	0.7	1.890	0.6
112	1.796	0.05	1.796	0.05	1.795	0.1
211	1.593	0.7	1.595	0.6	1.599	0.3
103	1.483	0.07	1.483	0.07	1.484	0

as reported in the previous studies, isotropic extended Sn 5s orbitals largely contribute to the VBM of SnO and form effective carrier conduction paths,[7,10] implying the possibility of the resonance bonding forming between Sn atoms. Consequently, it is concluded that the crystallization of SnO thin films establishes the long-range ordering, enhances the local polarizability, and resultantly increases the refractive index.

As Fig. 2 depicted, along with the transformation from SnO to SnO_2, a sharp drop in n is observed, which is associated with the smaller n of SnO_2. The polarizability is related to the ionicity of the chemical bond and the deformation of the electron cloud.[44] The interplay of polarizability and ionicity in IV-VI compounds has been investigated within a diatomic linear-chain model by Bussmann-Holder.[45] The Watson model and the closure approximation were used for the calculation of polarizability $p(r)$, which corresponds to[45]

$$p(r) = \frac{\langle 0|e^2r^2|0\rangle}{\Delta E_{\text{eff}}} \quad [3]$$

with $|0\rangle$ denoting the Watson sphere ground state for the equivalent radius r and ΔE_{eff} representing an effective gap. The resulting polarizability and the ionicity are directly related to each other by the following formula[45]

$$p(r) \cong \frac{M}{2\upsilon_A}\left(\frac{r'_\sigma + 1}{r'_\sigma}\right) \quad [4]$$

where $M = \langle 0|e^2r^2|0\rangle$, r'_σ is the ionicity, $r'_\sigma = (2\upsilon_A - \Delta E_{\text{eff}})/\Delta E_{\text{eff}}$, and υ_A is the atomic pseudopotential. It is suggested that the energy difference of p-orbital states of cation (Sn) and anion (O) gives the main contribution to the ionicity; i.e., r'_σ is approximately proportional to the energy gap between the upper valence band state ε_p^O and the lower conduction band state ε_p^{Sn}.[45] From band structure calculation, the p-band scheme $\varepsilon_p^O - \varepsilon_p^{Sn}$ for SnO_2 is larger than that for SnO,[10,46] which means the smaller polarizability of the former. Therefore, SnO_2 should exhibit a relatively small n (the reported value of n for SnO_2 is ~1.8 to 2.2)[24,30,33] compared with SnO, giving rise to a decreasing trend of n with the transformation from SnO to SnO_2.

Figure 3 plots the optical bandgaps (E_g) of all the films, which were arranged in the three phase regions. E_g was calculated using the following equation

$$(\alpha h\nu)^2 = A(h\nu - E_g) \quad [5]$$

where A is a constant and α is the absorption coefficient, which can be obtained via $\alpha = 4\pi k/\lambda$. The calculated E_g values of polycrystalline SnO films are ~2.68 to 2.78, which agree well with the epitaxial SnO films (~2.75 eV).[7] However, the E_g values of amorphous SnO films are ~3.36 to 3.51, which are a little out of the reported scope for SnO (2.5–3.4 eV). The bandgaps of films RTA-450 and RTA-500 are ~3.25 and ~3.31 eV, respectively, corresponding to the optical bandgaps of SnO_2 with SnO impurity phase involved.[47]

Figure 3 also summarizes the n values at $\lambda = 550$ nm and the energy values associated with the n maximum (E_n). The variation of E_n follows an opposite trend with that of n. Moreover, the covariation of n and E_g for the amorphous and polycrystalline SnO films can be manifested with the Moss rule. This semiempirical relation-

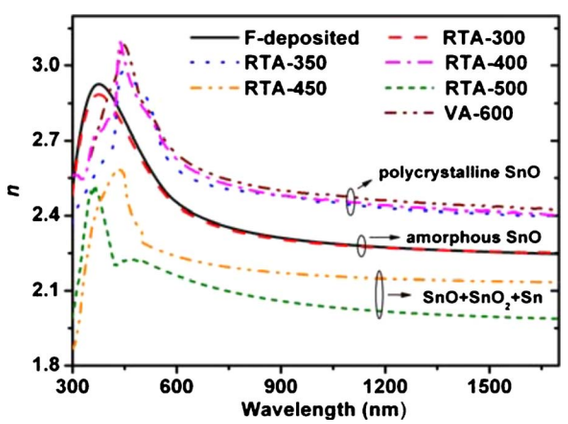

Figure 2. (Color online) Refractive index n vs wavelength for the obtained films.

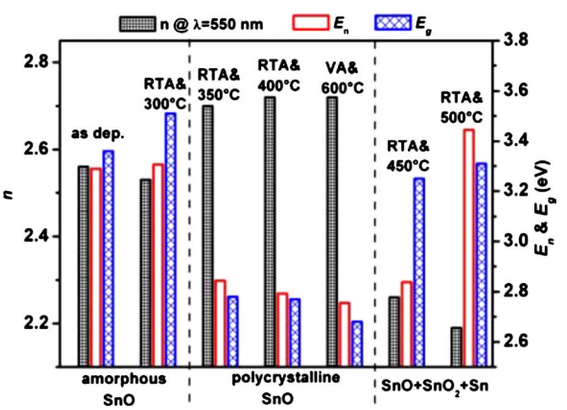

Figure 3. (Color online) The refractive index n values at $\lambda = 550$ nm, the energy values associated with the n maximum E_n, and the bandgaps E_g for the obtained films arranged in the three phase regions. The post-thermal treatment conditions are also listed correspondingly.

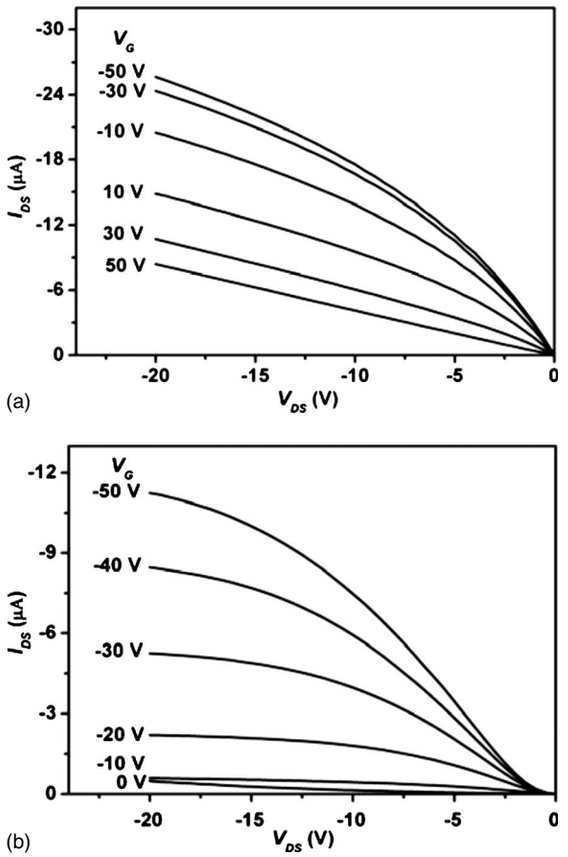

Figure 4. The characteristics of drain–source current (I_{DS}) vs drain–source voltage (V_{DS}) of the TFTs with (a) the RTA-350 channel and (b) the RTA-400 channel.

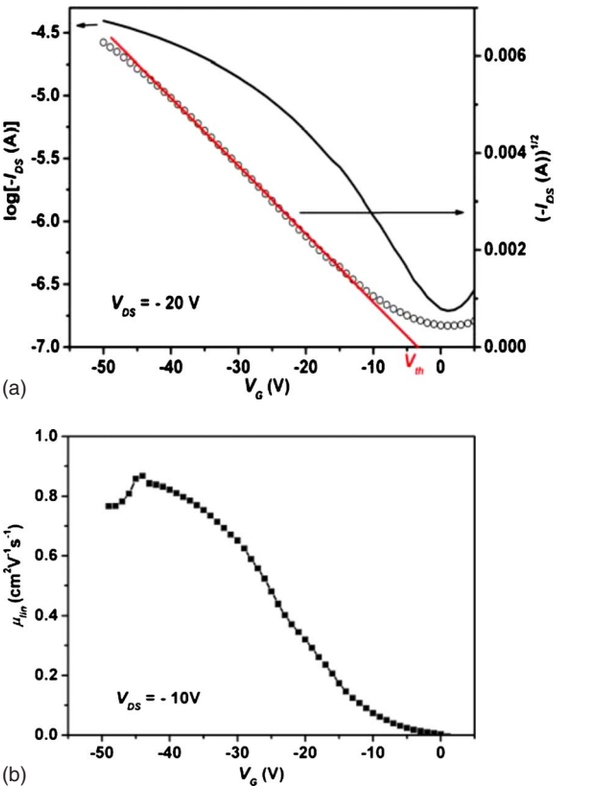

Figure 5. (Color online) (a) Transfer characteristics of the TFT with the RTA-400 channel at $V_{DS} = -20$ V. The straight line was plotted to obtain V_{th}. (b) Field-effect mobility in the linear region (μ_{lin} at $V_{DS} = -10$ V) as a function of V_G.

ship is based on the fundamental principle that in a dielectrics or semiconductor medium all energy levels are scaled down by a factor of square of the dielectric constant (ε^2) or by a fourth power of the refractive index (n^4), which can be expressed as[48]

$$n^4 E_g = \text{const} \quad [6]$$

In the present case, the constant was 90 ± 2 eV at λ = 1700 nm and 144 ± 4 eV at λ = 550 nm. The covariation of n and E_g for SnO films indicates that the dispersion of both of them can be ascribed to the variation of the local polarizability, which couples with microstructure changes.

TFT application.— According to the output characteristics, only the TFTs employing films RTA-350 and RTA-400 (polycrystalline SnO films) as channels exhibit p-type field effect transistor characteristics and the other four TFTs do not exhibit the gate effect, which is related to the electrical properties of the channels. For the amorphous F-deposited and RTA-300 channels, the conduction paths are fragmented and carriers are rather localized in the disordered structure, yielding a resistivity of as high as $\sim 10^4$ Ω cm. The poor electrical properties of the amorphous SnO channels would ruin the TFT performance eventually, which is similar to the case of some n-type TFTs.[49,50] As for the RTA-450 and RTA-500 channels, high densities of electrons (2×10^{19} and 5×10^{19} cm^{-3}, respectively) examined by the Hall effect measurement arise from the transformation from SnO to SnO_2 with the expulsion of Sn atoms,[24,36] rendering the channels too conductive (resistivity <0.1 Ω cm) to show the gate effect.

Figure 4 shows the output curves of the TFTs employing polycrystalline SnO channels. Both devices exhibit p-type field effect transistor characteristics: negative V_G increases $|I_{DS}|$ conspicuously, whereas positive V_G decreases $|I_{DS}|$ and depletes the channel carriers. However, the SnO TFT with the RTA-350 channel demonstrates a high off-current (~ 5 μA) and a small on/off current ratio (~ 10). The possible reason of the high off-current is that the hole density ($\sim 1 \times 10^{18}$ cm^{-3}) in the SnO channel is so large that it is difficult to deplete the channel. In contrast, the SnO TFT with the RTA-400 channel demonstrates the best performance. Good saturation of the drain–source current was clearly observed in the pinch-off region, in accordance with the theory of standard field effect transistors. A higher annealing temperature can improve the SnO crystallinity to some extent according to the XRD, resultantly reduces the amount of trap states, and then promotes the hole mobility (the Hall mobility of the RTA-400 channel is up to 1.6 cm^2 V^{-1} s^{-1} and has an enhancement of around two times of that of the RTA-350 channel), leading to the improved electrical properties of the TFT with the RTA-400 channel. However, it should be pointed out that I_{DS} curves are not linear around $V_G \sim 0$ V in the output characteristics of the TFT with the RTA-400 channel, revealing that the Ni/Au source–drain electrodes are not good ohmic contacts. Further investigation on it is in progress.

Figure 5a depicts the transfer characteristics of the TFT with the RTA-400 channel at $V_{DS} = -20$ V. The S value, the on/off current ratio, and the V_{th} estimated from the measured transfer curve are ~ 11 V/decade, ~ 200, and approximately -3.5 V, respectively. Therefore, the SnO TFT operates in the p-type enhancement mode. The turn-on voltage V_{on}, i.e., the gate voltage at which $|I_{DS}|$ begins to increase in a transfer characteristic, is positive (~ 1 V), and the off-current at V_{on} is a bit high, ~ 200 nA. The possible origin of the high off-current is that too many extra trap states exist at the deep energy levels (>0.2 eV above the valence band), and the Fermi

level cannot raise by applying a larger positive V_G.[8] The field-effect mobilities in the linear regions ($V_{DS} = -10$ V) μ_{lin} increase from 0 to 0.87 $cm^2\ V^{-1}\ s^{-1}$ as V_G decreases from V_{on}($\sim$1 V) to the on state at -44 V and then levels off at $V_G < -44$ V (Fig. 5b). The increase in μ_{lin} at low $|V_G|$ is ascribed to trap filling in the TFT device, whereas the decrease in μ_{lin} at larger $|V_G|$ is attributed to the carrier scattering at the SnO–SiO_2 interface.[51] The saturation mobility μ_{sat} calculated from the measured transfer curve (open circle line in Fig. 5a) is 0.46 $cm^2\ V^{-1}\ s^{-1}$. The maximum μ_{lin} value and μ_{sat} are the same order of magnitude as those of epitaxial SnO TFTs (μ_{sat} = 0.7 $cm^2\ V^{-1}\ s^{-1}$ and μ_{lin} = 1.3 $cm^2\ V^{-1}\ s^{-1}$).[8]

Conclusions

Amorphous SnO films were prepared on quartz and 190 nm SiO_2/Si(001) by electron-beam evaporation at RT, followed by a subsequent RTA treatment in Ar ambient at temperatures between 300 and 500°C. XRD results show that the crystallizing and the disproportionation decomposition of SnO start at 350 and 450°C, respectively, and the availability of the products (o-SnO_2 and Sn) during the decomposition is quite different from the previous results. The studies on the optical properties reveal that, the refractive index increases after SnO is crystallized and decreases sharply after SnO is decomposed into SnO_2 and Sn, and the "Moss rule" law is suitable to describe the relationship between the refractive indexes and optical bandgaps of the SnO thin films. The local polarizability is suggested to play an important role in determining the optical properties of the SnO_x films. Bottom-gate-type TFTs employing the obtained films on the SiO_2/Si(001) substrates as channels were also fabricated and characterized. The TFTs employing polycrystalline SnO channels exhibit p-type field effect transistor characteristics, and comparable electrical properties with those reported for epitaxial SnO TFTs were achieved by choosing proper annealing conditions. Further improving the electrical properties of the SnO TFTs and constructing fully transparent SnO TFTs will be the next step in developing complementary and more practical circuits in display technology.

Acknowledgment

This work was partially supported by the key project of the Natural Science Foundation of Zhejiang province, People's Republic of China (grant no. 0804201051) and by the Special Foundation of the President of Chinese Academy of Sciences (grant no. 080421WA01).

References

1. A. Odani, A. Nimberger, B. Markovsky, E. Sominski, E. Levi, V. G. Kumar, A. Motiei, A. Gedanken, P. Dan, and D. Aurbach, *J. Power Sources*, **119–121**, 517 (2003).
2. P. X. Song and D. S. Wen, *J. Phys. Chem. C*, **113**, 13470 (2009).
3. J. Calderer, P. Molinas, J. Sueiras, E. Llobet, X. Vilanova, X. Correig, F. Masana, and A. Rodriguez, *Microelectron. Reliab.*, **40**, 807 (2000).
4. Z. H. Han, N. Guo, F. Q. Li, W. Q. Zhang, H. Q. Zhao, and Y. T. Qian, *Mater. Lett.*, **48**, 99 (2001).
5. X. Q. Pan and L. Fu, *J. Appl. Phys.*, **89**, 6048 (2001).
6. J. Geurts, S. Rau, W. Richter, and F. J. Schmitte, *Thin Solid Films*, **121**, 217 (1984).
7. Y. Ogo, H. Hiramatsu, K. Nomura, H. Yanagi, T. Kamiya, M. Hirano, and H. Hosono, *Appl. Phys. Lett.*, **93**, 032113 (2008).
8. Y. Ogo, H. Hiramatsu, K. Nomura, H. Yanagi, T. Kamiya, M. Kimura, M. Hirano, and H. Hosono, *Phys. Status Solidi A*, **206**, 2187 (2009).
9. A. Seko, A. Togo, F. Oba, and I. Tanaka, *Phys. Rev. Lett.*, **100**, 045702 (2008).
10. A. Togo, F. Oba, I. Tanaka, and K. Tatsumi, *Phys. Rev. B*, **74**, 195128 (2006).
11. D. Adler and J. Feinleib, *Phys. Rev. B*, **2**, 3112 (1970).
12. A. Tsukazaki, A. Ohtomo, T. Onuma, M. Ohtani, T. Makino, M. Sumiya, K. Ohtani, S. F. Chichibu, S. Fuke, Y. Segawa, et al., *Nature Mater.*, **4**, 42 (2005).
13. Z. Ji, L. Zhao, Z. P. He, Q. Zhou, and C. Chen, *Mater. Lett.*, **60**, 1387 (2006).
14. J. Ni, X. Zhao, X. Zheng, J. Zhao, and B. Liu, *Acta Mater.*, **57**, 278 (2009).
15. M. Taguchi, M. Matsunami, Y. Ishida, R. Eguchi, A. Chainani, Y. Takata, M. Yabashi, K. Tamasaku, Y. Nishino, T. Ishikawa, Y. Senba, H. Ohashi, and S. Shin, *Phys. Rev. Lett.*, **100**, 206401 (2008).
16. P. Schröer, P. Krüger, and J. Pollmann, *Phys. Rev. B*, **47**, 6971 (1993).
17. J. E. Jaffe, R. Pandey, and A. B. Kunz, *Phys. Rev. B*, **43**, 14030 (1991).
18. X. Q. Pan and L. Fu, *J. Electroceram.*, **7**, 35 (2001).
19. W. Guo, L. Fu, Y. Zhang, K. Zhang, G. Graham, L. Y. Liang, Z. M. Liu, H. T. Cao, and X. Q. Pan, *Appl. Phys. Lett.*, **96**, 042113 (2010).
20. C. W. Ou, Dhananjay, Z. Y. Ho, Y. C.Chuang, S. S. Cheng,M. C. Wu, K. C. Ho, and C. W. Chu, *Appl. Phys. Lett.*, **92**, 122113 (2008).
21. H. Shimotani, H. Suzuki, K. Ueno, M. Kawasaki, and Y. Iwasa, *Appl. Phys. Lett.*, **92**, 242107 (2008).
22. K. Matsuzaki, K. Nomura, H. Yanagi, T. Kamiya, M. Hirano, and H. Hosono, *Phys. Status Solidi A*, **206**, 2192 (2009).
23. G. M. Wu, J. Wang, X. F. Tang, M. Gu, L. Y. Chen, and J. Shen, *Acta Phys. Sin.*, **49**, 1015 (2000).
24. J. Isidorsson, C. G. Granqvist, K. von Rottkay, and M. Rubin, *Appl. Opt.*, **37**, 7334 (1998).
25. M. S. Moreno, G. Punte, G. Rigotti, R. C. Mercader, A. D. Weisz, and M. A. Blesa, *Solid State Ionics*, **144**, 81 (2001).
26. H. Giefers, F. Porsch, and G. Wortmann, *Solid State Ionics*, **176**, 199 (2005).
27. M. S. Moreno, R. C. Mercader, and A. G. Bibiloni, *J. Phys.: Condens. Matter*, **4**, 351 (1992).
28. S. Goldsmith, E. Cetinorgu, and R. L. Boxman, *Thin Solid Films*, **517**, 5146 (2009).
29. A. De and S. Ray, *J. Phys. D: Appl. Phys.*, **24**, 719 (1991).
30. R. Sivaramasubramaniam, M. R. Muhamad, and S. Radhakrishna, *Phys. Status Solidi A*, **136**, 215 (1993).
31. L. Y. Liang, Z. M. Liu, H. T. Cao and X. Q. Pan, *ACS Appl. Mater. Interfaces*, In press. [DOI: 10.1021/am900838z]
32. Q. H. Li, D. L. Zhu, W. J. Liu, Y. Liu, and X. C. Ma, *Appl. Surf. Sci.*, **254**, 2922 (2008).
33. P. D. Paulson and S. S. Hegedus, *J. Appl. Phys.*, **96**, 5469 (2004).
34. Y. C. Liu, J. H. Hsieh, and S. K. Tung, *Thin Solid Films*, **510**, 32 (2006).
35. C. H. Shek, J. K. L. Lai, G. M. Lin, Y. F. Zheng, and W. H. Liu, *J. Phys. Chem. Solids*, **58**, 13 (1997).
36. L. Kaplan, A. Benshalom, R. L. Boxman, S. Goldsmith, U. Rosenberg, and M. Nathan, *Thin Solid Films*, **253**, 1 (1994).
37. H. Y. Fan and S. A. Reid, *Chem. Mater.*, **15**, 564 (2003).
38. S. S. Pan, Y. X. Zhang, X. M. Teng, G. H. Li, and L. Li, *J. Appl. Phys.*, **103**, 093103 (2008).
39. M. Losurdo, D. Barreca, P. Capezzuto, G. Bruno, and E. Tondello, *Surf. Coat. Technol.*, **151–152**, 2 (2002).
40. H. L. Lu, G. Scarel, M. Alia, M. Fanciulli, S. J. Ding, and D. W. Zhang, *Appl. Phys. Lett.*, **92**, 222907 (2008).
41. R. D. Shannon, R. C. Shannon, O. Medenbach, and R. X. Fischer, *J. Phys. Chem. Ref. Data*, **31**, 931 (2002).
42. K. Shportko, S. Kremers, M. Woda, D. Lencer, J. Robertson, and M. Wuttig, *Nature Mater.*, **7**, 653 (2008).
43. P. B. Littlewood, *J. Phys. C*, **12**, 4459 (1979).
44. J. C. Phillips, *Rev. Mod. Phys.*, **42**, 317 (1970).
45. A. Bussmann-Holder, *Phys. Rev. B*, **40**, 11639 (1989).
46. Y. P. Du, J. C. Chen, and J. Feng, *Acta Phys.-Chim. Sin*, **25**, 278 (2009).
47. A. F. Khan, M. Mehmood, A. M. Rana, M. T. Bhatti, and A. Mahmood, *Chin. Phys. Lett.*, **26**, 077803 (2009).
48. N. K. Sahoo, S. Thakur, R. B. Tokas, A. Biswas, and N. M. Kamble, *Appl. Surf. Sci.*, **253**, 3455 (2007).
49. Dhananjay, S. S. Cheng, C. Y. Yang, C. W. Ou, Y. C. Chuang, M. C. Wu, and C. W. Chu, *J. Phys. D: Appl. Phys.*, **41**, 092006 (2008).
50. H. Z. Zhang, H. T. Cao, A. H. Chen, L. Y. Liang, Z. M. Liu, and Q. Wan, *Solid-State Electron.*, **54**, 479 (2010).
51. J. F. Wager, D. A. Keszler, and R. E. Presley, *Transparent Electronics*, 1st ed., Chap. 5, p. 130, Springer Science+Business Media, New York (2008).